JOURNAL OF PROPULSION AND POWER
Vol. 24, No. 2, March–April 2008

Multidimensional Numerical Simulation of Ammonium-Perchlorate-Based Propellant Combustion with Fine/Ultrafine Aluminum

L. Massa* and T. L. Jackson†
University of Illinois at Urbana–Champaign, Urbana, Illinois 61801

DOI: 10.2514/1.26728

This paper presents a computational investigation on the deflagration of composite ammonium-perchlorate-based propellant with fine/ultrafine aluminum. The model relies on an Eulerian representation of the particle cloud formed by the ejected aluminum and a gray-medium approximation of the radiative field supported by the emitting particles. The aluminum oxidation is modeled by means of an experimentally evaluated diameter power law valid for constant-ambient conditions. The energetic consequences of the addition of nanoscale aluminum are analyzed, with particular emphasis on the contributions of radiative transport and aluminum oxidation heat release. The model is validated versus experimental measurements of burn rates for both one-dimensionally (fine ammonium perchlorate) and three-dimensionally (monomodal and bimodal coarse ammonium perchlorate) supported combustion fields. The burn rate and surface shape of two-dimensional laminate propellant is also considered, and the particle consumption time is related to experimental observations.

Nomenclature

A	=	prefactor in the propellant burn-rate power law
c_p	=	specific heat at constant pressure
D	=	diameter
$\mathcal{D}$	=	effective diffusion coefficient
$D_{g,i}$	=	kinetics rates of preexponential terms
G	=	incident radiation
I	=	radiation intensity
I_b	=	blackbody intensity
J_w	=	radiosity
K_a	=	absorption coefficient
M	=	mass flow rate
K_s	=	scattering coefficient
K_v	=	diameter cofactor in the aluminum burn-rate law
K_{em}	=	total emission coefficient
m_i	=	kinetics rates of temperature exponents
N_s	=	number of species in the gas phase
n_i	=	kinetics rates of pressure exponents
P	=	chamber pressure
Q_s	=	condensed-phase heat release
$\boldsymbol{q}$	=	heat-flux vector
T	=	temperature
t	=	volume fraction
w	=	weight fraction
Y_k	=	mass fraction of the gas-phase species k
$\beta_{k,i}$	=	coefficients in the mass conservation
β_M	=	aluminum-oxide/aluminum molar mass ratio
β_ρ	=	aluminum-oxide/aluminum density ratio
γ_i	=	coefficients in the energy balance
ϵ	=	surface emissivity
θ_i	=	kinetics rates of scaled activation energy
λ	=	thermal conductivity
$\nu_{i,k}$	=	kinetics rates of species exponents
ρ	=	mass density
$\hat{\rho}$	=	surface reflectivity
σ_v	=	relative volume loss in aluminum particle burning
ϕ_v	=	calibration factor in the burn-rate law
ω	=	albedo

Subscripts

Al	=	aluminum
AP	=	ammonium perchlorate, oxidizer
B	=	binder matrix
blend	=	fine blend of oxidizer and fuel
c	=	conductive energy transfer
g	=	gas phase
HTPB	=	hydroxyl terminated polybutadiene, fuel
r	=	radiative energy transfer
s	=	solid phase

I. Introduction

IN THIS research, we are interested in the effect of aluminum particles on the deflagration characteristics of solid rocket propellants. The study is restricted to considering fine and ultrafine aluminum, which is assumed to be much smaller than any length scale of interest and thus does not require a particle-tracking strategy. Fine and ultrafine aluminum are defined here to be aluminum smaller than about 3 μm in diameter. We make no distinction in this range between micron size (less than 3 μm) and nano-size aluminum, and so the word *ultrafine* will be used to describe the whole range of aluminum encompassed in the model. The rationale for this choice is related to the insensitivity of the burning characteristics of randomly packed propellant to a decrease in aluminum particle diameter within the aforementioned range and for pressures in the operative range of aerospace motors (20–70 atm, Stephens et al. [1]). This phenomenon is discussed in detail in Sec. VIII. The ultrafine aluminum is added to the solid-phase binder to create a homogeneous blend of Al powder and binder.

Aluminum is added to the propellant for a variety of reasons, including acoustic stabilization and increased impulse. Both of these phenomena take advantage of the large heat release of the aluminum oxidation reaction in the gas chamber and do not relate to the propellant burning. Recently, experimental investigations by Dokhan et al. [2] showed that adding a small volume fraction of nanoscale aluminum to the propellant has a profound impact on the

Received 23 July 2006; revision received 25 July 2007; accepted for publication 25 July 2007.

*Research Scientist, Center for Simulation of Advanced Rockets; currently Visiting Professor, Clemson University; lmassa@clemson.edu. Member AIAA.

†Senior Research Scientist; tlj@csar.uiuc.edu. Associate Fellow AIAA.

deflagration process itself, by markedly increasing the propellant consumption rate. Regarding the combustion region close to the propellant surface, the role of the Al oxidation heat release on the surface thermal feedback is usually considered modest because of the high temperature necessary to initiate the aluminum oxidation, which is inhibited by the aluminum-oxide shell until it melts.

In addition to the heat of combustion, another important manner by which the aluminum enhances the propellant thermal feedback is the radiation field supported by the ejected particle cloud. Because the particles are very small, they can be considered to be at the same temperature as the surrounding gas and thus they emit strongly in a continuum spectrum above the infrared band. The radiation field has been studied in detail by Ishihara et al. [3] and Brewster and Parry [4]. Recently, Jackson et al. [5] showed that the high burn rates measured by Dokhan et al. [2] can be explained by considering a suitable radiation field, but neglecting heat release. In the present paper, we build upon such investigation and develop a model for heterogeneous propellant deflagration that includes both radiation and heat release. The investigation focuses on the effects of these two phenomena on the deflagration process.

The validation of the model as a means to predict the combustion characteristics of a composite propellant of aluminized ammonium perchlorate and hydroxyl terminated polybutadiene (AP/HTPB) is carried out in three steps. First, we perform a comparison between the model and experiments for the burn rate of propellant that supports a 1D combustion field. The fine AP propellant mixes of Dokhan et al. [2] are considered. Second, the model is applied to study the combustion field supported by the sandwich propellant (i.e., 2D laminate propellant characterized by a steady deflagration process). Finally, the computational analysis is validated by carrying out predictions for randomly packed propellant that supports a multidimensional unsteady (3D) deflagration process and combustion field. The average regression speeds for three coarse AP propellant mixes are compared with the experiments of Stephens et al. [1] in the pressure range of 22–68 atm.

The paper is organized as follows: the radiative heat transfer equations and their interaction with the transport and chemical processes are introduced in Secs. II and III, the aluminum oxidation model is detailed in Secs. IV and V, the three steps of the validation are discussed in Secs. VI, VII, and VIII, and the conclusions and an overview of future works are presented in Sec. IX.

II. Radiative Transfer Equations

The cloud formed by the fine/ultrafine particles is modeled, from the radiative standpoint, as a gray medium with time–space-varying emission and absorption characteristics. In this section, the radiative heat transfer equation for the cloud will be derived. The derivation assumes that the propellant surface lies in the x–y plane and burns in the nominal z direction.

The radiative transfer equation (RTE) for a gray medium is given by

$$\boldsymbol{s}\cdot\nabla I+(K_s+K_a)I=K_{\mathrm{em}}I_b+\frac{K_s}{4\pi}\int_{4\pi}I\Phi\,\mathrm{d}\Omega' \tag{1}$$

$$\nabla=\left(\frac{\partial}{\partial x},\frac{\partial}{\partial y},\frac{\partial}{\partial z}\right) \tag{2}$$

$$\int_{4\pi}\mathrm{d}\Omega'=\int_{\phi'=0}^{2\pi}\int_{\theta'=0}^{\pi}\sin\theta'\,\mathrm{d}\theta'\,\mathrm{d}\phi' \tag{3}$$

where $I=I(\boldsymbol{r},\boldsymbol{s})$ is the intensity that depends on position and direction, $\Phi=\Phi(\boldsymbol{s},\boldsymbol{s}')$ is the scattering phase function, $\boldsymbol{r}=(x,y,z)$ is the position vector, and $\boldsymbol{s}=(s_x,s_y,s_z)$ denotes the direction cosines

$$s_x=\sin\theta\cos\phi,\qquad s_y=\sin\theta\sin\phi,\qquad s_z=\cos\theta \tag{4}$$

where $0\le\theta\le\pi$ is the polar angle with respect to the z axis, $0\le\phi\le2\pi$ is the azimuthal angle with respect to the x–y plane, and the blackbody intensity I_b is given by

$$I_b=\sigma T^4/\pi \tag{5}$$

with $\sigma=5.67\times10^{-12}\ \mathrm{W/cm^2\cdot K^4}$, the Stefan–Boltzmann constant. The preceding parameters are the scattering coefficient K_s, the absorption coefficient K_a, and the total emission coefficient K_{em}.

The incident radiation G and the radiative heat-flux vector $\boldsymbol{q}$ are defined as

$$G(\boldsymbol{r})=\int_{4\pi}I(\boldsymbol{r},\boldsymbol{s}')\,\mathrm{d}\Omega' \tag{6}$$

$$\boldsymbol{q}(\boldsymbol{r})=\int_{4\pi}I(\boldsymbol{r},\boldsymbol{s}')\boldsymbol{s}'\,\mathrm{d}\Omega' \tag{7}$$

Our model makes a number of assumptions:

Assumption 1: The particulate-mixture cloud can be modeled as a gray medium; the radiative properties (absorption and scattering) are independent of the spectral wave number.

Assumption 2: The propellant is opaque (i.e., the transmissivity τ is zero).

Assumption 3: We ignore in-depth absorption at the surface.

Assumption 4: The propellant surface is a diffuse-gray surface and, as such, it emits and reflects diffusely (i.e., the exiting intensity is independent of direction); then

$$I(\boldsymbol{r}_w,\boldsymbol{s})=J_w(\boldsymbol{r}_w)/\pi,\qquad \boldsymbol{n}\cdot\boldsymbol{s}>0$$

where

$$J_w=\epsilon\pi I_b+\hat{\rho}H \tag{8}$$

is the surface radiosity and the subscript w denotes a value on the propellant surface. Here, H is the hemispherical irradiation (i.e., incoming radiative heat flux):

$$H(\boldsymbol{r}_w)=\int_{\boldsymbol{n}\cdot\boldsymbol{s}'<0}I(\boldsymbol{r}_w,\boldsymbol{s})|\boldsymbol{n}\cdot\boldsymbol{s}'|\,\mathrm{d}\Omega'$$

where $\boldsymbol{n}$ is the local outward normal, and $\boldsymbol{n}\cdot\boldsymbol{s}'=\cos\theta'$ is the cosine of the angle between any incoming direction $\boldsymbol{s}'$ and the surface normal.

Assumption 5: The intensity is periodic in the x and y directions (the propellant burns downward in the nominal $-z$ direction).

Assumption 6: The phase scattering function is taken to be linear anisotropic:

$$\Phi(\boldsymbol{s},\boldsymbol{s}')=1+A_1\boldsymbol{s}\cdot\boldsymbol{s}'$$

Setting $A_1=0$ implies isentropic scattering. However, Brewster and Parry [4] noted that smoke is anisotropic and so we allow for this possibility.

Most, if not all, of the assumptions can be relaxed if more information about the radiation field is known. In any event, we wish to begin the model within the simplest possible framework.

To solve the radiative transfer equation (1), we use the P_1 approximation of the spherical harmonics method, which is equivalent to the first-moment method. We begin by writing for the intensity

$$I(\boldsymbol{r},\boldsymbol{s})=a(\boldsymbol{r})+\boldsymbol{b}(\boldsymbol{r})\cdot s \tag{9}$$

Substituting Eq. (9) into Eqs. (6) and (7) yields the relations

$$G=4\pi a,\qquad \boldsymbol{q}=\frac{4\pi}{3}\boldsymbol{b} \tag{10}$$

which in turn yields for the intensity

$$I(\boldsymbol{r},\boldsymbol{s}) = \frac{1}{4\pi}[G(\boldsymbol{r}) + 3\boldsymbol{q}(\boldsymbol{r})\cdot\boldsymbol{s}] \tag{11}$$

In deriving these relations, we used the following identities:

$$\int_{4\pi} \mathrm{d}\Omega' = 4\pi, \qquad \int_{4\pi} \boldsymbol{s}'\,\mathrm{d}\Omega' = 0, \qquad \int_{4\pi} \boldsymbol{s}'\boldsymbol{s}'\,\mathrm{d}\Omega' = \frac{4\pi}{3}\mathcal{I} \tag{12}$$

where $\mathcal{I}$ is the unit tensor. The integral on the right-hand side of the RTE (1) then becomes

$$\int_{4\pi} I(\boldsymbol{r},\boldsymbol{s}')\Phi(\boldsymbol{s},\boldsymbol{s}')\,\mathrm{d}\Omega' = G + A_1\boldsymbol{q}\cdot\boldsymbol{s} \tag{13}$$

Substituting the intensity (11) into Eq (1), multiplying by $(1, \boldsymbol{s})$, and integrating each equation over all solid angles yields the following two relations:

$$\nabla\cdot\boldsymbol{q} = 4\pi K_{\mathrm{em}} I_b - K_a G =: R \tag{14}$$

$$\nabla G = -(K_s + K_a)[3 - A_1\omega]\boldsymbol{q} =: P\boldsymbol{q} \tag{15}$$

where $\omega = K_s/(K_s + K_a)$ is the albedo. These last two relations are combined to yield a single equation for G in conservation form:

$$2\nabla^2 G - \frac{\nabla\cdot P\nabla G}{P} = PR \tag{16}$$

This equation, subject to appropriate boundary conditions that will be defined subsequently, is to be solved numerically in the gas phase, together with the zero-Mach-number reactive equations. Once G is known, the radiative heat flux is given by

$$\boldsymbol{q} = \frac{-1}{(K_s + K_a)(3 - A_1\omega)}\nabla G \tag{17}$$

and in the energy equation, we have

$$\nabla\cdot\boldsymbol{q} = 4\pi K_{\mathrm{em}} I_b - K_a G \tag{18}$$

(see the discussion in Modest [6], page 475).

For the boundary condition at the propellant surface, we require that such a boundary condition is satisfied in an integral sense (see the discussion in Modest [6], p. 470). The analysis starts by writing for the intensity along the propellant surface:

$$I(\boldsymbol{r} = \boldsymbol{r}_w, \boldsymbol{s}) = I_w(\boldsymbol{r}_w, \boldsymbol{s}) \tag{19}$$

for $\boldsymbol{n}\cdot\boldsymbol{s} > 0$ (i.e., the intensity leaving a surface must be prescribed in some fashion for all outgoing directions $\boldsymbol{n}\cdot\boldsymbol{s} > 0$). This relation is, of course, general, in that it applies in all cases. Using Assumption 4, that the surface emits and reflects diffusely, the preceding reduces to

$$I(\boldsymbol{r} = \boldsymbol{r}_w, \boldsymbol{s}) = I_w(\boldsymbol{s}) \quad \text{for } \boldsymbol{n}\cdot\boldsymbol{s} > 0 \tag{20}$$

Evaluating Eq. (11) on the surface, multiplying by $\boldsymbol{s}\cdot\boldsymbol{n}$, and integrating over the hemisphere yields

$$\int_{\boldsymbol{n}\cdot\boldsymbol{s}>0} I_w(\boldsymbol{s})\boldsymbol{s}\cdot\boldsymbol{n}\,\mathrm{d}\Omega = \frac{1}{4\pi}\int_{\boldsymbol{n}\cdot\boldsymbol{s}>0} (G + 3\boldsymbol{q}\cdot\boldsymbol{s})\boldsymbol{s}\cdot\boldsymbol{n}\,\mathrm{d}\Omega \tag{21}$$

Let

$$\boldsymbol{q}\cdot\boldsymbol{s} = q_{t1}\sin\theta\cos\phi + q_{t2}\sin\theta\sin\phi + q_n\cos\theta$$

where (q_{t1}, q_{t2}) are the tangent components and q_n is the normal component, and recall that $\boldsymbol{s}\cdot\boldsymbol{n} = \cos\theta$. Substitution yields

$$\int_{\boldsymbol{n}\cdot\boldsymbol{s}>0} I_w(\boldsymbol{s})\boldsymbol{s}\cdot\boldsymbol{n}\,\mathrm{d}\Omega = \frac{1}{4}(G + 2q_n) \tag{22}$$

or

$$G + 2q_n = 4\int_{\boldsymbol{n}\cdot\boldsymbol{s}>0} I_w(\boldsymbol{s})\boldsymbol{s}\cdot\boldsymbol{n}\,\mathrm{d}\Omega \tag{23}$$

Substituting Assumption 4 for the intensity in terms of the surface radiosity yields

$$G + 2q_n = 4J_w \tag{24}$$

In addition to this relation, we require that the normal radiative heat flux is the sum of the incident and reflected (radiosity) contributions:

$$q_n = J_w - H \tag{25}$$

The incident radiation is eliminated in favor of the radiosity using Eq. (8), and the hemispherical reflectivity is related to the absorptivity α by the Kirchhoff law for diffuse-gray surfaces,

$$\hat{\rho} = 1 - \alpha \tag{26}$$

to yield

$$q_n = \frac{\epsilon\pi I_b - \alpha J_w}{1 - \alpha} \tag{27}$$

We use Eqs. (24) and (27) to eliminate J_w, yielding

$$2q_n = \frac{1}{2 - \alpha}[4\epsilon\pi I_b - \alpha G] \tag{28}$$

Substituting Eq. (17) to eliminate $\boldsymbol{q}$ yields the proper boundary condition along the propellant surface:

$$\frac{-2n\cdot\nabla G}{(K_s + K_a)(3 - A_1\omega)} = \frac{1}{2 - \alpha}4\epsilon\pi I_b - \alpha G \tag{29}$$

This is an implicit boundary condition for the unknown function G (i.e., a Robin boundary condition).

The other boundary conditions assume either periodicity for randomly packed propellants or zero normal fluxes for sandwich propellants. G is periodic at

$$x = \pm L_x, \qquad y = \pm L_y \tag{30a}$$

$$\frac{\partial G}{\partial x} = 0 \quad \text{at } x = \pm L_x, \qquad Gy = 0 \quad \text{at } y = \pm L_y \tag{30b}$$

and far away from the propellant surface, the radiation field is in equilibrium

$$\boldsymbol{q} \to 0 \Rightarrow \nabla G \to 0 \quad \text{as } z \to \infty \tag{31}$$

To summarize, we solve Eq. (16) for the incident radiation G, subject to the boundary conditions (29–31). Once G has been determined, the radiative heat flux $\boldsymbol{q}$ can be found from Eq. (17). The unknown parameters that must be modeled are K_s, K_a, K_{em}, A_1, α, and ϵ.

III. Interaction with the Combustion Field and Parameters

Radiation affects the combustion field through the radiative heat contribution, $\nabla\cdot q \equiv -\nabla\cdot q_r$, and it affects the connection conditions at the propellant surface because of the term q_n in Eq. (27). The propellant surface is considered to be an opaque surface, in the sense that no radiation penetrates into the solid phase (i.e., all is absorbed at the surface). Thus, no changes are necessary to the solid-heat-conduction equation. We note, however, that the presence of aluminum does affect the heat conduction in the solid, mainly because of changes in thermal conductivity of the aluminum fuel blend. This effect is accounted for by using homogenization formulas as discussed by Jackson et al. [5]. These formulas will be described in more detail later in this manuscript.

A. Gas Phase

In this subsection, we briefly outline the gas-phase equation to highlight the changes due to the presence of the radiative field.

Consider a reacting mixture composed of N_s species that can react according to N_r reaction steps. Let T denote the gas-phase temperature and let Y_i, $i = 1, \ldots, N_s$ denote the gas-phase species mass fractions. The equations expressing conservation of energy and species mass in a nonconservative form are

$$\rho c_p \frac{\mathrm{D}T}{\mathrm{D}t} - \frac{\mathrm{d}P}{\mathrm{d}t} = -\nabla \cdot \boldsymbol{q} + \sum_{i=1}^{N_r} \gamma_i R_i \tag{32a}$$

$$\rho \frac{\mathrm{D}Y_k}{\mathrm{D}t} = \nabla \cdot \left(\frac{\lambda}{c_p} \nabla Y_k \right) + \sum_{i=1}^{N_r} \beta_{k,i} R_i \qquad k = 1, \ldots, N_s \tag{32b}$$

where $\beta_{k,i}$ and γ_i are coefficients based upon mass and total enthalpy conservation, respectively, that are fully determined given a particular reaction scheme. The reaction steps are expressed in general form as

$$R_i = D_{g,i} P^{n_i} T^{m_i} \prod_{k=1}^{N_s} Y_k^{\nu_{i,k}} \exp(-\theta_i / T) \tag{33}$$

where $D_{g,i}$ is the gas-phase Damköhler number for species i; P is the leading-order pressure in a small-Mach-number expansion and can, at most, be a function of time; and θ_i the gas-phase activation temperature for species i. For global kinetics, the species exponent $\nu_{i,k}$ in the reaction rates need not be related to the stoichiometric coefficients of the corresponding reaction; their values are assigned by matching reaction rate constants with experiments. The parameters of the combustion model ($D_{g,i}$, n_i, m_i, $\nu_{i,k}$, and θ_i) are calibrated using a global optimization strategy discussed by Massa et al. [7]. The values of the combustion model parameters are identical to those reported in Jackson et al. [5].

In addition, ρ is the density, c_p is the specific heat assumed to be independent of the composition, λ is the gas-phase thermal conductivity taken to be a function of the temperature and the volume fraction of aluminum and aluminum oxide (Al_2O_3) in the gas phase, and $\boldsymbol{q}$ the heat-flux vector. The formalisms defining the thermoinertial properties of the multiphase flow will be defined in detail in Sec. IV. In writing down these equations, the Lewis number for each species was assumed to be unity, and second-order-or-higher terms in the Mach number were neglected. The heat-flux vector is the sum of a conductive part and a radiative part:

$$\boldsymbol{q} = \boldsymbol{q}_c + \boldsymbol{q}_r \tag{34}$$

where the conductive part is assumed to obey Fourier's law:

$$\boldsymbol{q}_c = -\lambda \nabla T \tag{35}$$

and the radiative part is given in the previous section:

$$\boldsymbol{q}_r = \frac{-1}{(K_s + K_a)(3 - A_1 \omega)} \nabla G \tag{36}$$

and

$$\nabla \cdot \boldsymbol{q}_r = 4\pi K_{em} I_b - K_a G \tag{37}$$

Recall that I_b is the blackbody radiation

$$I_b = \frac{\sigma}{\pi} T^4 \tag{38}$$

and the incident radiation term G is governed by Eq. (16).

Mass diffusion is neglected in the solid phase, so that the energy conservation reduces to the heat conduction equation for a heterogeneous solid:

$$\rho_s c_p T t = -\nabla \cdot \boldsymbol{q_c} \tag{39}$$

The thermal properties of the solid phase are assumed to be dependent on the material, but independent of the state (pressure/temperature).

The convective transport in Eq. (32) is approximated by using the Oseen approximation, which does not require the solution of the fluid-dynamic part of the low-Mach-number Navier–Stokes equations. The basic assumption of the Oseen approximation is that the stream tubes are vertical, with a constant cross-sectional area. When applied to multidimensional deflagrating propellant with a corrugated surface, the mass flux within each stream tube is found by accounting for the total volume of propellant swept by the regressing front. The 3D computational analysis of Massa et al. [8] demonstrated that the relative burn-rate error computed comparing predictions from the Oseen and the Navier–Stokes approximations is lower than 10%, well within the measurement error bars. More detail on the application of such approximation to propellant deflagration analysis can be found in Jackson and Buckmaster [9].

B. Connection Conditions

The connection conditions at the propellant surface relate the solution in the solid phase to that in the gas phase. The burning interface is treated as a reacting regressing sheet separating the two phases. The temperature, the normal mass flux, and the tangential velocity are continuous across the sheet, so that if $\boldsymbol{n}$ is the surface normal pointing into the gas

$$[T] = 0 \tag{40}$$

$$[M] = [\rho(\boldsymbol{u} \cdot \boldsymbol{n} + r_b)] = 0 \tag{41}$$

$$[\boldsymbol{u} \times \boldsymbol{n}] = 0 \tag{42}$$

The energy balance and the species mass balance across the interface become

$$[-\boldsymbol{n} \cdot \boldsymbol{q}] = -Q_s M \tag{43}$$

$$\left[\frac{\lambda}{c_p} \boldsymbol{n} \cdot \nabla Y_i \right] = M[Y_i] \tag{44}$$

The jump operator in the preceding equations is defined as $[\cdot] = (\cdot)_g - (\cdot)_c$. If we eliminate the heat-flux vector in the energy balance in terms of the corresponding conductive and radiative parts, then we get

$$[\lambda \boldsymbol{n} \cdot \nabla T] = \boldsymbol{n} \cdot \boldsymbol{q}_r|_g - Q_s M \tag{45}$$

or, upon using Eq. (28),

$$[\lambda \boldsymbol{n} \cdot \nabla T] = \frac{1}{2(2 - \alpha)} (4\pi I_b - \alpha G) - Q_s M \tag{46}$$

We note that the phase-change heat release Q_s is a function of space along the surface, according to

$$Q_s = \begin{cases} Q_{s,\mathrm{AP}} & \psi = 1 \\ Q_{s,\mathrm{blend}} & \psi = -1 \end{cases} \tag{47}$$

where ψ is a time and space function that takes the value of 1 if a point is located on the AP surface and -1 if is located elsewhere. For the blend, we have

$$Q_{s,\mathrm{blend}} = w_{\mathrm{AP}} Q_{s,\mathrm{AP}} + w_{\mathrm{Al}} Q_{s,\mathrm{Al}} + w_B Q_{s,B} \tag{48}$$

where w_i ($i = \mathrm{AP}, \mathrm{Al}, B$) are the weight fractions of the blend that is the component i. Here, $w_{\mathrm{AP}} + w_{\mathrm{Al}} + w_B = 1$. Because aluminum does not pyrolyze, we set $Q_{s,\mathrm{Al}} = 0$.

C. Radiation Parameters

The radiation model is an adaption of the model used by Brewster and Parry [4] for conventional-size aluminum and used in our previous study of a blend of fine AP and aluminum [5]. Thus, the contribution of the particles is accounted for by setting

$$K_a = \frac{3t_{\text{oxide}}\alpha_{\text{oxide}}}{D_{\text{oxide}}} + k_1\frac{3t_{\text{Al}}\alpha_{\text{Al}}}{D_{\text{Al}}}$$
$$K_s = \frac{3t_{\text{oxide}}\hat{\rho}_{\text{oxide}}}{D_{\text{oxide}}} + k_1\frac{3t_{\text{Al}}\hat{\rho}_{\text{Al}}}{D_{\text{Al}}} \tag{49}$$
$$K_{\text{em}} = \frac{3t_{\text{oxide}}\epsilon_{\text{oxide}}}{D_{\text{oxide}}} + k_1\frac{3t_{\text{Al}}\epsilon_{\text{Al}}}{D_{\text{Al}}}$$

where t_{Al} and t_{oxide} are the volume fractions of aluminum and aluminum oxide, respectively, in the gas-phase; α, $\hat{\rho}$, and ϵ are the absorptivity, reflectivity, and emissivity, respectively; and k_1 is an empirical constant that reflects uncertainties in the evaluation of the diameter of the aluminum particles. In the simulations discussed in this paper, this parameter was set to unity.

The average diameter of the injected particles can be much larger than the average diameter of the initial distribution of aluminum, due to the possibility of agglomeration. Agglomeration is a phenomenon that depends on the aluminum particles' surface residence time, which in turn depends on the propellant burn rate [10]. For burn rates typical of composite propellant with ultrafine aluminum, the residence time is short and agglomeration effects must be considered negligible. The experimental investigation of Stephens et al. [1] showed that changing the size of aluminum from 3 μm to nano-size aluminum does not alter the burn rate for monomodal 200-μm-diam AP. However, the addition of 36-μm aluminum sharply reduces the propellant burn rate when the overall volume fraction of metal is maintained constant. Consequently, all simulations discussed in this work assume that the initial diameter of the particle ejected in the gas phase is $D_0 = 3$ μm, corresponding to the upper boundary of the fine/ultrafine range as it was defined in the Introduction.

Other model uncertainties include the values of α_{Al}, $\hat{\rho}_{\text{Al}}$, and ϵ_{Al}, as well as the diameter D_{oxide}. The values of the constants used in this study are given in Table 1 and are taken from Brewster and Parry [4]. The diameter of aluminum and oxide particles are determined by solving for Eulerian fields representative of the dispersed gas–particulate mixture; this topic is discussed in detail in the next section.

The parameters listed in Eq. (49) are identical to those used by Jackson et al. [5] and consider the contribution of the particles only. The contribution of the gas mixture is accounted for by evaluating the effective absorption coefficient for the gray gas as the Planck-mean absorption coefficient $K_{p,\text{gas}}$ (Modest [6], page 344). $K_{p,\text{gas}}$ should, in principle, be determined by integrating the spectral absorption coefficient of the gas over the relevant bands. The result of this calculation would be temperature-, pressure-, and composition-dependent. Because of the absence of a detailed kinetic mechanism in our model, only the pressure dependence is retained:

$$K_{p,\text{gas}} = \kappa_{p,\text{gas}}P \tag{50}$$

Assuming the combustion products to be composed in large part of CO_2, we select the value $\kappa_{p,\text{gas}} = 0.3\ (\text{cm}\cdot\text{atm})^{-1}$, based upon the results of Zhang and Modest [11]. For the gas–particulate mixture, the coefficients are determined by augmenting K_a and K_{em} in Eq. (49) by the contribution $K_{p,\text{gas}}$.

Table 1 Radiation parameter values from Brewster and Parry [4]

	α	$\hat{\rho}$	ϵ	D, μm
Al	0.10	0.90	1.00	1.0
Al_2O_3	0.45	0.55	0.45	0.3

IV. Aluminum Modeling

The presence of aluminum in the solid phase is accounted for by evaluating the density, thermal conductivity, and pyrolysis rate according to homogenization formula derived for a fine binder–aluminum blend. Most of the homogenization formulas are dictated by conservation principles, and their derivation is straightforward. The expression for the thermal conductivity does not stem from a conservation argument. The formulas used in this research are identical to those described by Jackson et al. [5],

$$1 = (1 - t_{\text{Al}})^3\left(\frac{1 - (\lambda_{\text{Al}}/\lambda_{\text{HTPB}})}{(\lambda_{\text{blend}}/\lambda_{\text{HTPB}}) - (\lambda_{\text{Al}}/\lambda_{\text{HTPB}})}\right)^3\frac{\lambda_{\text{blend}}}{\lambda_{\text{HTPB}}} \tag{51}$$

where blend identifies the fuel–aluminum mix in the solid. Likewise, in the gas phase, the thermal conductivity is evaluated from homogenization formulas which are formally identical to those in the solid phase [Eq. (51)] and require knowledge of the gas and particulate thermal conductivities and gas-phase volume fractions.

The presence of aluminum in the gas phase is modeled by defining a set of continuous Eulerian fields that describe the particle transport as a subscale phenomenon of the gas-phase microscale processes: those based upon morphological length scales.

The aluminum in the gas phase is present either as liquid aluminum or solid/liquid aluminum oxide. These two states are connected along the global chemical path:

$$\text{Al}\,(s) + m\text{OX} \rightarrow \tfrac{1}{2}\text{Al}_2\text{O}_3(s/l) + \text{ products} \tag{52}$$

where OX typifies oxidizing species in the product stream and m is equal to $3/2$ divided by the number of oxygen atoms in OX. The aluminum reacts with the hot oxidizing species away from the surface because of the inhibiting effect of the oxide shell. Therefore, OX includes the oxygen-rich species in the equilibrium gas products of the AP/HTPB combustion. If we assume the specific heat of reactants and products to be equal, the heat release can be found based upon the heat of formation of the species. Hence, if $\text{OX} = \text{O}_2$ in Eq. (52), the associated heat release is $Q_{\text{Al}} = 7165$ cal/g, whereas if $\text{OX} = \text{H}_2\text{O}$, the heat release is $Q_{\text{Al}} = 3957$ cal/g; note that this value is per gram of aluminum and that the aluminum oxide is assumed to be in the liquid state. Based upon equilibrium chemistry calculation, by matching flame temperatures for a AP/HTPB/Al homogenized blend, we select the value to be closer to the latter, and we set $Q_{\text{Al}} = 4500$ cal/g.

Given that the fields are modeled as Eulerian fields, we now introduce the concept of Eulerian density of the nanoscale condensed phases and distinguish it from the Lagrangian density, which is constant and equal to the material value. The Eulerian density is defined as the ratio of the mass of condensed matter to the extension of the volume that contains it, when the volume is taken smaller than all the relevant physical scales. The Eulerian densities $\tilde{\rho}_{\text{Al}}$ and $\tilde{\rho}_{\text{oxide}}$ are related to the Lagrangian counterparts $\rho_{\text{Al,oxide}}$ by

$$\tilde{\rho}_{\text{Al,oxide}} = \rho_{\text{Al,oxide}}t_{\text{Al,oxide}} \tag{53}$$

where $t_{\text{Al,oxide}}$ are the volume fractions of aluminum and aluminum oxide, respectively, in the gas phase. Also, we note that the overall density is

$$\rho = \tilde{\rho}_{\text{oxide}} + \tilde{\rho}_{\text{Al}} + \rho_{\text{gas}} \tag{54}$$

where the density of the gas is found from Dalton's law for a mixture of perfect gases:

$$\rho_{\text{gas}} = \frac{P}{RT}(1 - t_{\text{Al}} - t_{\text{oxide}}) \tag{55}$$

Finally, the mass fractions of the dispersed particle phase are

$$Y_{\text{Al,oxide}} = \frac{\tilde{\rho}_{\text{Al,oxide}}}{\rho} \tag{56}$$

The preceding formulas yield a modified thermal equation of state in which the mass fractions of the particulate field modulate the

pure-gas equation. Specifically, in terms of the Lagrangian densities of the particulate, its mass fractions, the chamber pressure, and the temperature,

$$\rho = \frac{p}{RT}\left(1 + Y_{\mathrm{Al}}\left(\frac{p}{RT\rho_{\mathrm{Al}}} - 1\right) + Y_{\mathrm{oxide}}\left(\frac{p}{RT\rho_{\mathrm{oxide}}} - 1\right)\right)^{-1} \tag{57}$$

The transport equations for the Eulerian fields are

$$\rho\frac{\mathrm{D}Y_{\mathrm{Al,oxide}}}{\mathrm{D}t} = \nabla\cdot\left(\mathcal{D}_{\mathrm{Al,oxide}}\nabla Y_{\mathrm{Al,oxide}}\right) + \dot{\omega}_{\mathrm{Al,oxide}} \tag{58}$$

where $\mathcal{D}$ is a diffusion coefficient that models the motion of the particles with respect to the gas flow due to concentration gradients, a phenomenon necessary to maintain spatial continuity of the concentration fields. Its value is assumed to be very small and is taken to be the 15th part of the diffusion coefficient of the gaseous species. This is a convenient value because it corresponds to the minimum value necessary to obtain convergence of the multigrid Poisson solver for the radiative heat equation. Simulations have demonstrated insensitivity to this parameter, however, and therefore it has not been selected for a parametric study. The term $\dot{\omega}$ in Eq. (58) represents the mass conversion of aluminum to alumina and is determined from the aluminum-burning model discussed in detail in the following section. Note that once the mass fractions are calculated, the diameter of the particles is evaluated as

$$D_{\mathrm{Al}} = D_o\left(\frac{Y_{\mathrm{Al}}\beta_M}{Y_{\mathrm{Al}}\beta_M + Y_{\mathrm{oxide}}}\right)^{1/3} \tag{59a}$$

$$D_{\mathrm{oxide}} = D_o\left(\frac{Y_{\mathrm{oxide}}}{Y_{\mathrm{Al}}\beta_M + Y_{\mathrm{oxide}}}\frac{\beta_M}{\beta_\rho}\right)^{1/3} \tag{59b}$$

where $\beta_\rho = \rho_{\mathrm{oxide}}/\rho_{\mathrm{Al}}$, $\beta_M = M_{\mathrm{oxide}}/(2M_{\mathrm{Al}})$ (with M being the molecular weight), and D_o is the initial diameter of the particles as they are ejected from the surface.

V. Aluminum Burning

A. Model

The burning of aluminum spheres is modeled using a power law representation of the volume consumption of the particles in a constant-property environment:

$$\sigma_v := \frac{1}{V}\frac{\mathrm{d}V}{\mathrm{d}t} = -k_v D_{\mathrm{Al}}^{-n} \tag{60}$$

where the exponent n is commonly assumed to be close to two, and the cofactor k_v is dependent on the local conditions, such as temperature, pressure, and oxidizing-species concentration. The exponent and cofactor can be obtained from experimentally measured particle burnout times if the surrounding conditions are assumed to be invariant of time. Experimental correlations are usually presented as

$$t_{\mathrm{burnout}} = k_b D_o^{n_d} T^{-n_t} P^{-n_p} \chi_{\mathrm{ox}}^{-n_o} \mathcal{D}_{\mathrm{rel}}^{-1} \tag{61}$$

where χ_{ox} is the concentration of oxidizing species active along the path equation (52) and $\mathcal{D}_{\mathrm{rel}}$ is a diffusion parameter (see the discussion in Najjar et al. [12] for more details). Time integrating between the initial time and the burnout time yields the relations

$$n = n_d \tag{62}$$

$$k_v = \frac{3}{k_b n} T^{n_t} P^{n_p} \chi_{\mathrm{ox}}^{n_o} \mathcal{D}_{\mathrm{rel}} \tag{63}$$

The value of k_b obtained by different experimental procedures can differ by several orders of magnitude. No power law exists that is valid in the entire range of aluminum diameters of interest to solid propellant analysis.

Another modeling uncertainty is rooted in the fact that aluminum near the surface burns differently before and after the oxide shell breakup. For microscale particles, the shell breakup is commonly identified with the melt temperature of the aluminum oxide, $T_{\mathrm{melt,oxide}} = 2350$ K; for nanoscale particles, the formation and resealing of cracks makes this definition more ambiguous. Below such transitional temperature, the microscale aluminum is assumed to undergo negligible oxidation. On the contrary, nanoscale particles are considered to undergo significant oxidation at a temperature below that of the shell breakup, at approximately the aluminum melting temperature [13,14]. Experiments by Bazyn et al. [15] showed that the burnout time of nanoscale particles is essentially temperature-insensitive for ambient values lower than approximately 2000 K, whereas it sharply decreases by an order in magnitude above such a temperature, demonstrating the presence of the two stages of burning in nanoscale aluminum. The first stage, for $T < T_{\mathrm{melt,oxide}}$, is characterized as the core-shrinking phase of the burning, a strictly diffusion-limited and temperature-independent process (Aita et al. [16]); the reason that the core-shrinking phase is not important at the microscale level is the larger volume/surface ratio of the particles. The second stage, valid after the oxide shell breaks, is more complex and its model should take into account aluminum kinetics paths.

The Widener and Beckstead [17] model offers the best available correlation for the full combustion stage of aluminum burning. This correlation was obtained for micron-size aluminum, and so it does not necessarily extend to the nanoscale range. By using the Widener and Beckstead correlation, we set $k_b = 1138$, $n_t = 1.57$, $n_p = 0.2$, and $n_o = 0.39$, and the dimensions are taken to be Kelvin, atmosphere, and microns. Because of the significant disparity in the burnout times between the two stages of burning, the core-shrinking stage is disregarded, by effectively setting $k_v = 0$ when the temperature is lower than the melting temperature of the oxide.

Experiments by Bazyn et al. [15] showed that the temperature overshoot above ambient of the aluminum particle in constant-ambient-condition experiments is limited by the dissociation of alumina. To reproduce this phenomenon, aluminum burning is turned off when the gas temperature reaches the boiling point of the Al_2O_3. The average value for the aluminum-oxide boiling point in the pressure range $P \in 20$–70 atm is taken to be $T_{\mathrm{boil,oxide}} = 4100$ K. These considerations yield a transformed particle burning law:

$$\sigma_v = \begin{cases} -k_v D_{\mathrm{Al}}^{-n} & T_{\mathrm{melt,oxide}} < T < T_{\mathrm{boil,oxide}} \\ 0 & T < T_{\mathrm{melt,oxide}}, T > T_{\mathrm{boil,oxide}} \end{cases} \tag{64}$$

Equation (64) is then used to evaluate the source terms in Eq. (58), resulting in the formalisms

$$\dot{\omega}_{\mathrm{Al}} = \rho Y_{\mathrm{Al}}\sigma_v \tag{65a}$$

$$\dot{\omega}_{\mathrm{oxide}} = -\dot{\omega}_{\mathrm{Al}}\beta_M \tag{65b}$$

B. Uncertainty and Parametric Study

Because of the high degree of uncertainty in the burning formulas a parametric study will be conducted by premultiplying k_v by a factor, denoted in the following as ϕ_v,

$$k_v = \frac{3\phi_v}{k_b n} T^{n_t} P^{n_p} \chi_{\mathrm{ox}}^{n_o} \mathcal{D}_{\mathrm{rel}} \tag{66}$$

The factor will be varied by effectively calibrating the model versus lower-dimension (1D and 2D) experimental data. The calibration shows ϕ_v to be always less than one to obtain sensible results, demonstrating that microscale burn-rate correlations overpredicts the burn rate of nanoscale particles.

VI. One-Dimensional Burning Propellant with Fine/Ultrafine Aluminum

Jackson et al. [5] showed that the burn rate of 1D propellant can be matched by using radiative/nonburning aluminum spheres if assumptions are made on the radiative parameters. Here, we extend the aforementioned analysis and investigate the importance of aluminum combustion on the 1D regression rates. To this end, the uncertainty parameter of the aluminum burning is varied in the interval $\phi_v \in [7.8125 \times 10^{-3}, 1]$. The results are compared with the experiments of Dokhan et al. [2], who correlated the burn rate of aluminized propellant to the mass fraction of ultrafine aluminum.

For the comparison presented in this section, two propellant formulations were selected, which correspond to the experimental denominations M28 and M29 of Table 2. The comparison between experiments and predictions is showcased in Fig. 1, in which a set of burn-rate–pressure lines at constant ϕ_v is plotted; ϕ_v is successively halved. The outcome that the experimental data points are located in the r_b–P plane along lines at constant ϕ_v suggests that varying a single parameter might be sufficient to calibrate the model. The optimal value of ϕ_v, that which minimizes the L_2 norm of the relative error, falls between 0.125 and 0.25 (the line for $\phi_v = 0.125$ is not shown in Fig. 1, to limit the number of lines in the plot).

Two observations are of note regarding the use of the experiments of Dokhan et al. [2] as calibration data. First, aluminum volume fractions in the propellant mixes of Table 2 are decisively lower than those found in industrial propellant, so that calibrating our model versus this set of experiments might not be representative of the range of aluminum fraction used in engineering applications and in the heterogeneous propellant validation presented later. Second, the 1D experiments have a very low oxidizer mass fraction (last column of Table 2). In this range, the global chemistry model, which assumes a linear variation of the flame temperature with the oxidizer solid content, decidedly overpredicts the adiabatic flame temperature of the propellant.

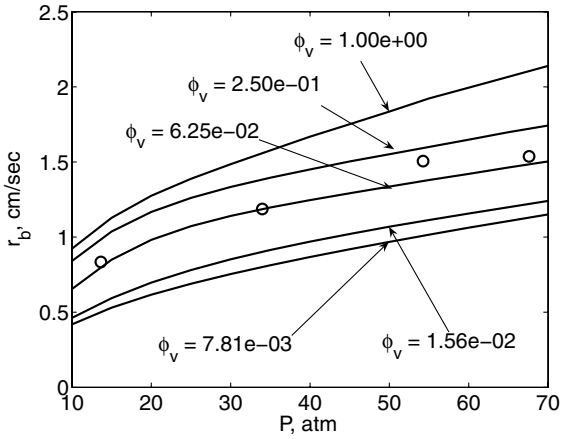

a) M28

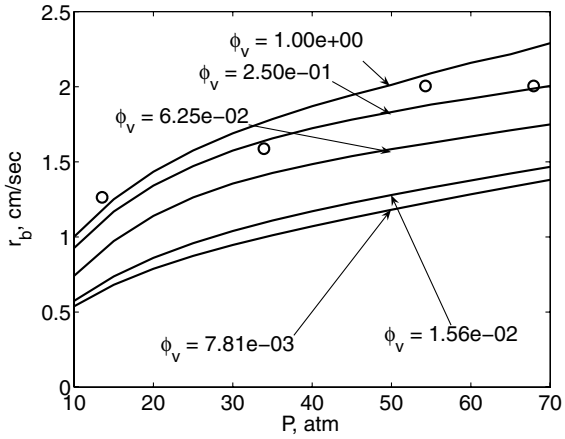

b) M29

Fig. 1 One-dimensional solutions correlated with variations of the aluminum burning parameter ϕ_v; open circles are the experimental measurements of Dokhan et al. [2].

VII. Sandwich

The steady-state burning behavior of adiabatic sandwiches is investigated in this section. Steady-state solutions are determined by pseudotime relaxation of the gas-phase time-dependent processes [Eq. (32)], with the solid thermal field and surface shape determined at each computational time step by solving the steady-state form of the respective governing equations. The multigrid technique (see, for example, Brandt [18]), coupled with the generalized minimal residual algorithm method (Saad and Schultz [19]) is used to solve the linear systems of equations arising from the discretization of the partial differential equations.

The sandwiches are stoichiometric with respect to the oxidizer–fuel ratio, whereas the volume fraction of aluminum is varied. Aluminum volume fractions corresponding to the cases M28 and M29 in Table 2 are considered. The cases will be denoted with respect to the aluminum solid content as M28 stoichiometric (M28s) and M29 stoichiometric (M29s). The sandwiches have a fuel-aluminum core and two slabs of AP on the sides. The thickness of the sandwich is set to 0.8 mm, so that varying the percentage of aluminum varies the binder/aluminum core thickness: 0.217 mm for M28s and 0.213 mm for M29s. Zero-flux boundary conditions are used for the side boundary conditions.

Presented results include the sandwich surface shape, the burn rate, and the aluminum particles' consumption time. We remark that the sandwich surface is an important parameter in the analysis of propellant combustion because it carries information about heat-flux distribution on the surface. The particle consumption time is defined in this context as the time at which the particle volume reduces to $1/100$ of its injection value.

A. Grid Convergence

A grid convergence study is performed on M28s, with $\phi_v = 0.15$ and at the pressure of 22 atm. The domain height is set to 1.5 mm. The grids are uniformly spaced in the direction perpendicular to the nominal regression and exponentially spaced in the direction of the burning; the exponential grid distribution is varied with pressure, and surface clustering is accentuated when pressure is increased. The code uses second-order centered-finite-difference operators for the diffusive terms and second-order total-variation-diminishing operators for the convective terms. Two computational meshes are considered: the fine grid has 320×120 points in both the solid and gas phases, whereas for the coarse mesh, the number of points in each computational coordinate was halved to 160×60. The results of the test are shown in Fig. 2. The difference between the two shapes is considered to be insignificant to the scope of this research, and the

Table 2 Mass and volume percentages of the matrix components

	Binder %		AP %		Al %		$m_{AP}/(m_{AP} + m_{HTPB})$
Matrix[a]	Mass	Volume	Mass	Volume	Mass	Volume	
M28	25.58	42.92	66.05	52.29	8.37	4.79	.72
M29	21.96	37.97	70.86	57.80	7.18	4.23	.76

[a]The matrix comprises fine AP and ultrafine aluminum embedded in the fuel binder.

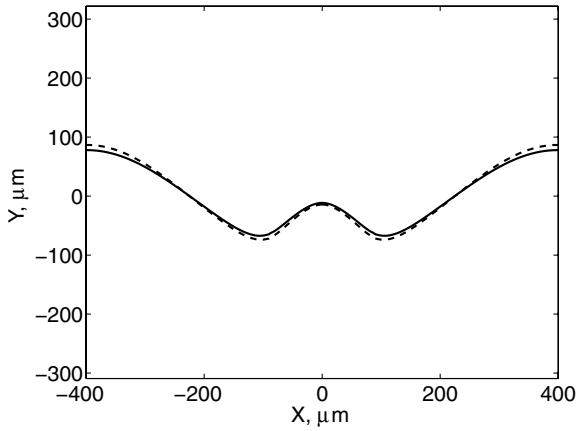

Fig. 2 Grid convergence study for steadily burning sandwiches; the solid line is the fine mesh and the dashed line is the coarse mesh.

intermediate mesh (240 × 100) is selected to carry out the numerical experiments documented in the next section. The relative error based on the difference between the regression rates computed with the two grids is ≈1.8%. Note that convergence of the surface shape and regression rate is a good representation of the overall convergence of the solution, because the exponential (Arrhenius) representation of the (surface) pyrolysis processes acts to accentuate temperature and mass fraction errors of finite difference approximations.

B. Sandwich Results

1. Burning and Radiation

The first set of results deals with the calibration of the aluminum burning model and is based on the correlation between results and the uncertainty parameter ϕ_v. The pressure is fixed at 22 atm. The shape for M28 and M29 stoichiometric sandwiches is shown in Fig. 3. For the same cases, the sandwich burn rate is plotted versus the uncertainty factor ϕ_v in Fig. 4. In Fig. 5, the particle consumption time is plotted versus the x coordinate at which a particle is injected. Clearly, the upper and lower abscissa limits in Fig. 5 identify the binder thickness.

Values of the consumption time can be compared with constant-ambient-condition measurements to provide a qualitative assessment of the model prediction. Bazyn et al. [20] measured consumption times on the order of 400–600 μs for 10-μm particles in an argon gas mixture at 2650 K, 15 atm, and with a molar fraction of H_2O equal to 0.5. Bazyn et al. noted that the burn time is weakly dependent on the ambient pressure. When comparing the results of Fig. 5 with constant-ambient-condition experiments, it should be considered that disregarding the oxidation of aluminum below $T_{\text{melt,oxide}}$ leads to an overprediction of the consumption time. The large error bars on the experimental data and the lack of a complete set of measurements makes it impossible to calibrate burn-rate law based on matching experimental data for consumption time only. The considerations discussed in this section, together with the burn-rate comparison of Fig. 1, lead to selecting $\phi_{v,b} = 0.15$ as the baseline value of the uncertainty parameter.

In Figs. 6 and 7, the gas-phase fields for the baseline case ($\phi_v = \phi_{v,b}$) are plotted for M28s and M29s, respectively. The contour plots show that the radiation contributes to the energy balance by transferring energy from the region of high temperature at the flame core to the relatively colder regions at the propellant surface. Also of note is the fact that the volume fraction of aluminum diminishes from its maximum value at the binder–gas interface because of two phenomena: initially, in the low-temperature region, because of the effect of gas acceleration on mass conservation, and finally, further from the surface, because of the aluminum oxidation. The former phenomenon is associated with the increased interparticle distances caused by the increased flow velocity and supports the idea that agglomeration might occur in the gas phase, but close to the surface.

The set of results presented in Figs. 3–7 reveals the strong influence of the aluminum burning on the combustion field. By

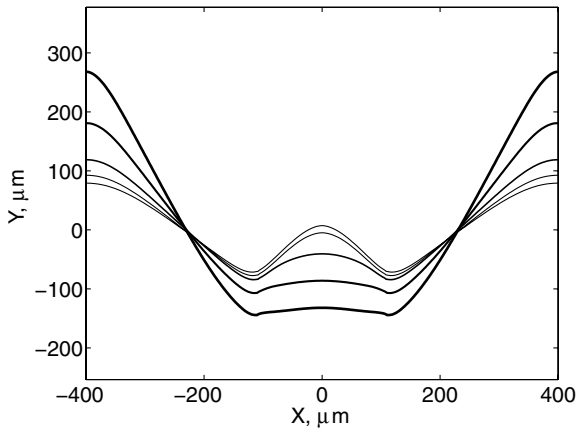

a) M28, stoichiometric

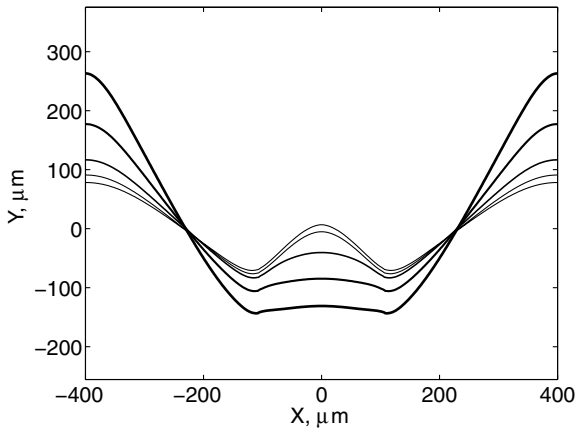

b) M29, stoichiometric

Fig. 3 Sandwich shape for two values of solid aluminum content; pressure is set to 22 atm; lines of increasing thickness identify increasing values of ϕ_v in the set $\phi_v \in \{0.0625, 0.125, 0.25, 0.5, 1\}$.

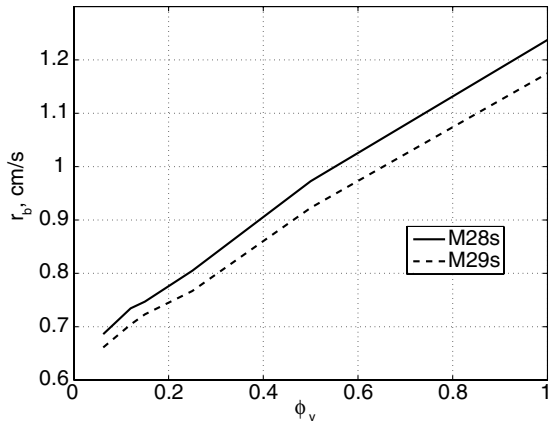

Fig. 4 Sandwich burn rate for two values of solid aluminum content; pressure is set to 22 atm.

increasing the parameter ϕ_v, the core of the sandwich recedes more pronouncedly and the binder surface tends to become flat, an observation in agreement with the experiments of Mullen and Brewster [21]. Note that a comparison with the work of Mullen and Brewster can be made only at the qualitative level, because they used an AP/HTPB/Al blend for the core, with aluminum particles of 15 μm in diameter. The recession of the binder core is significantly larger for aluminized propellants than for nonaluminized propellants. The burn rate of the sandwiches is also strongly affected by the particle burning. Moreover, a comparison between

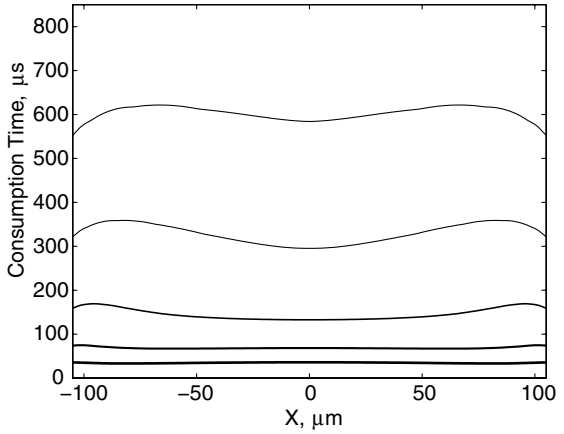

a) M28, stoichiometric

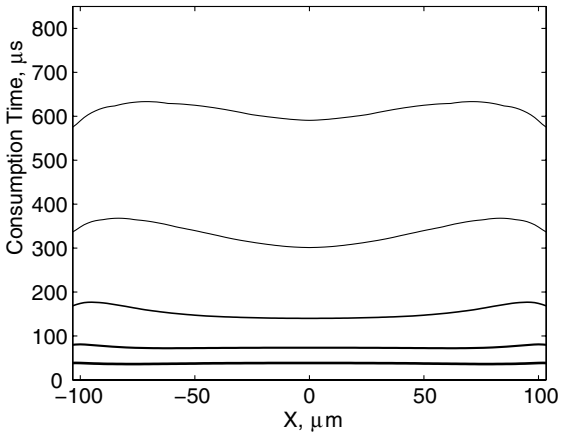

b) M29, stoichiometric

Fig. 5 Aluminum particles consumption time in sandwich propellant for two values of solid aluminum content; lines of increasing thickness identify increasing values of ϕ_v in similar fashion to Fig. 3; pressure is set to 22 atm.

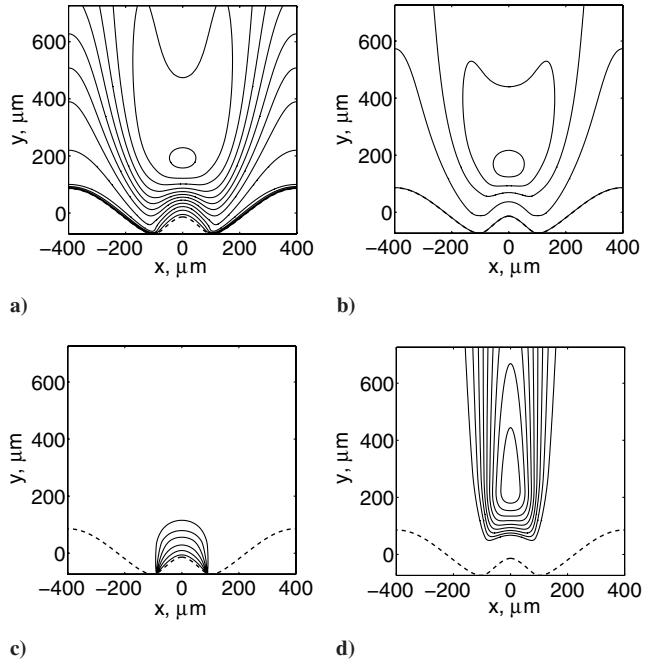

Fig. 6 Steadily burning sandwich M28s at 22 atm and $\phi_v = 0.15$: a) $T \in [885, 4850]$ K, b) $-\nabla \cdot q_r \in [-22, 5.7]$ Kcal cm^{-3} s^{-1}, c) $t_{\mathrm{Al}} \in [0, 3.8 \times 10^{-3}]$, and d) $t_{\mathrm{oxide}} \in [0, 1.1 \times 10^{-4}]$; there are 20 equally spaced contours within the limits.

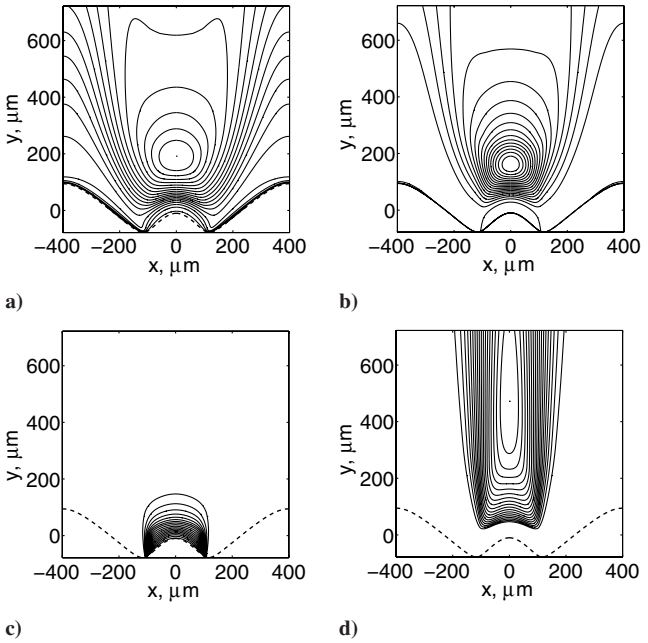

Fig. 7 Steadily burning sandwich M29s at 22 atm and $\phi_v = 0.15$: a) T, K, b) $-\nabla \cdot q_r$ Kcal cm^{-3} s^{-1}, c) t_{Al}, and d) t_{oxide}; contours are the same as in Fig. 6.

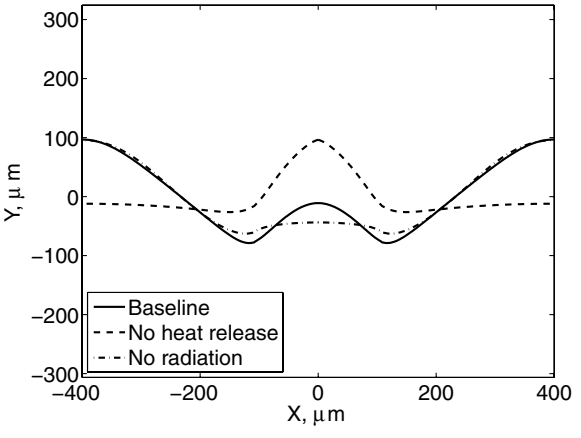

a) Shape

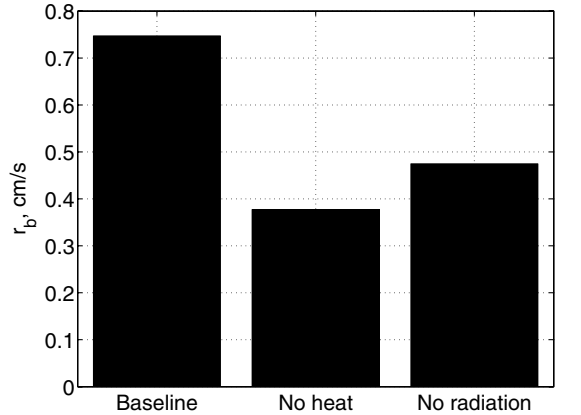

b) Burn rate

Fig. 8 Sandwich shape and burn rate for M28s at 22 atm, when either the radiation field or the aluminum burning was turned off.

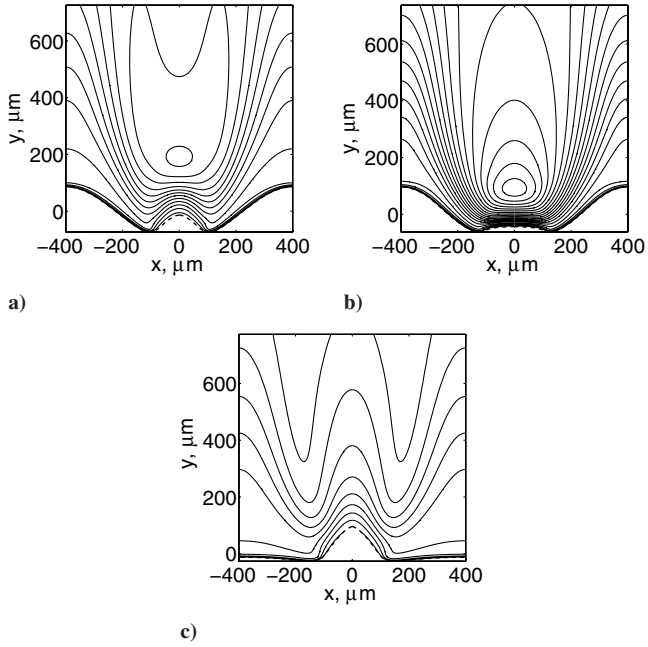

Fig. 9 Radiation and burning aluminum contributions to the temperature field for the M28s sandwich at 22 atm: a) radiating burning aluminum, b) nonradiating burning aluminum, and c) radiating nonburning aluminum; there are 20 equally spaced contours between 885 and 4850 K.

results for M28s and M29s reveals that increasing the aluminum content increases both burn rate and binder recession.

It is of interest to separate the contribution of the radiative field from that of the particle burning by performing simulations in which we turn off radiation and heat release separately. The results of such simulations are detailed in Fig. 8, in which the case in which both radiation and aluminum burning are included is denoted as the baseline. The figure shows that the burn rate is significantly reduced by the removal of either the radiation field or the heat release (i.e., both are important energetic contributions). By examining Fig. 8a, the conclusion is drawn that the heat released by the aluminum oxidation acts to produce a flatter binder profile, a consequence of the premixed nature of aluminum combustion in the fine/ultrafine range, which leads to a large amount of heat being released over the whole binder region. Radiation, on the other hand, produces an even distribution of heat release over the entire AP/binder propellant surface, a consequence of the elliptic smoothness of the operator that controls radiative heat transfer. The radiation contribution does not significantly change the binder protrusion from that characteristic of a nonaluminized propellant. These concepts are substantiated by investigating the temperature fields for three cases: baseline, only burning, and only radiating aluminum. Such a comparison is presented in Fig. 9. The thermal field displays an interesting change in the combustion field structure. For the only radiative case, the leading-edge flamelet mechanism dominates the combustion fields; the binder tapered protrusion reflects the heat distribution typical of the Beckstead et al. [22] flame system; the low temperature of the flame diminishes the emission from the flame considerably. For the burning nonradiative case, the heat release from the aluminum oxidation dominates the thermal field. The heat release is concentrated in the binder region, and a flat binder shape is the result.

2. *Pressure Effects*

Variation of the sandwich shape and burn rate with the pressure for the baseline case is shown in Fig. 10a, showing the M28s shape, and in Fig. 10b, showing the burn rates for both propellant mixes. An increase in pressure has the effect of decreasing the binder recession similarly to the nonaluminized propellant case (cf. Massa et al. [23]). Higher aluminum solid loadings lead to a more pronounced recession at low pressure, at which the sandwich shape (recessed

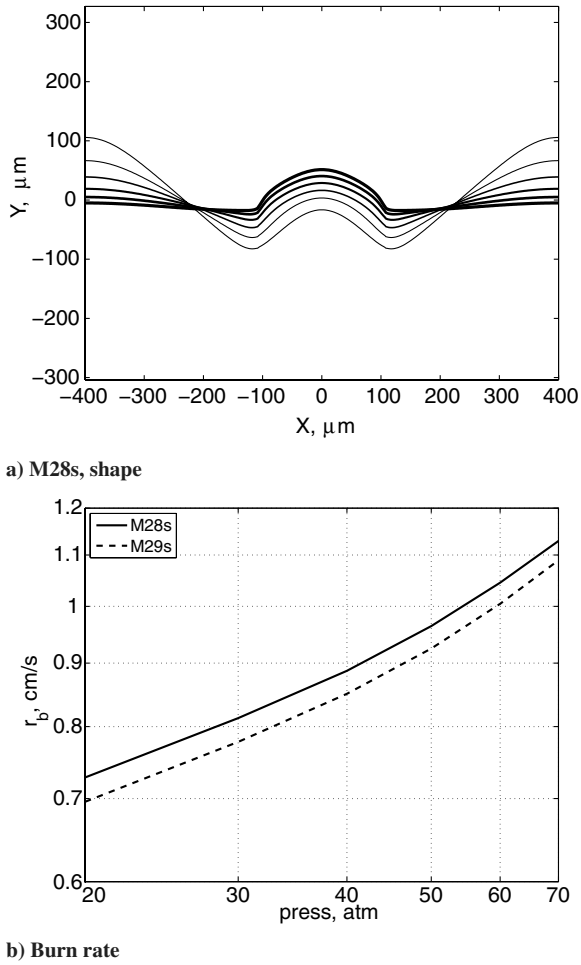

Fig. 10 Dependence of sandwich shape and burn rate on the pressure. In Fig. 10a, lines of increasing thickness identify increasing values of P in the set $P \in \{20, 30, 40, 50, 60, 70\}$ atm.

binder) indicates that the oxidizer/binder flame has a larger contribution to the energetic balance than the AP decomposition flame. On the other hand, for a pressure greater than 60 atm, the sandwich surface heat feedback is dominated by the AP monopropellant flame contribution, and the shape of the AP surface changes from convex to concave. This curvature effect indicates that heat flow is transferred within the solid phase from the AP region far from the binder lamina to the AP/binder interface, and the sandwich burn rate is lower than the pure AP value. The difference between the burning rate of M28s and M29s decreases with an increase in pressure (Fig. 10b), revealing a diminishing importance of aluminum combustion to the overall burn rate. Nonetheless, at high pressure, the binder protrusion is less marked than for nonaluminized sandwiches (cf. Massa et al. [23]), and so the aluminum oxidation is an important source of heat feedback to the binder region. The burn-rate–pressure exponent $\partial \log r_b / \partial \log P$ varies in the range of 0.2745–0.5235 for the results presented in Fig. 10b.

The variation of the particle burnout time with the pressure is shown in Fig. 11. Three points are of note about the results shown in this figure. First, each curve correlating the consumption time with the surface departure location has a global minimum at $X = 0$, the sandwich centerline; the depth of the minimum increases with the pressure. This phenomenon is linked to the effect of pressure on the sandwich shape. As the pressure increases, the tip of the binder tends to protrude from the AP and moves closer to the hot final-diffusion flame, to keep up with the AP deflagration. The final diffusion flame is that identified with the reaction of AP combustion products (result of the premixed combustion of AP dissociation products) and binder gases that were not consumed in the direct reaction with AP dissociation products (primary diffusion flame). Thus, aluminum

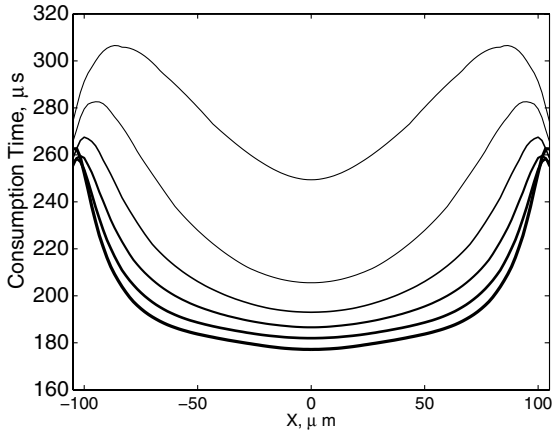

Fig. 11 Particle burn time over the surface for M28s at different pressures. The thickness of the lines increases with the pressure in the same fashion as in Fig. 10.

particles leaving the surface close to the sandwich centerline travel the shortest distance before reaching the hottest region of the flowfield. Second, consumption times at low pressure have a local maximum at a departure location close to the AP/binder interface. This outcome is explained by considering the large localized heat output of the primary diffusion flame, which yields a local maximum in gas temperature. Third, the consumption time for particles departing from the AP/binder interface decreases as the pressure increases. This phenomenon is explained by considering the reduction in flow velocity at the gas side of the burning surface as a consequence of the increase in density: at high pressure, aluminum particles reside for a longer time in the cool region close to the binder surface. The increased time necessary to reach the final diffusion flame at high pressure suggests an increased importance of the core-shrinking (aluminum) burn law for $P > 50$ atm.

VIII. Three-Dimensional Randomly Packed Propellant

A. Experimental Data

Stephens et al. [1] performed a systematic study of aluminum in AP-based randomly packed composite propellants. Most of the work was for fine and ultrafine aluminum, although a few cases with 36-μm aluminum was also studied. We restrict our attention to those cases containing fine and ultrafine aluminum. Table 3 outlines information about each of the propellant mixes studied in the experimental study. A few comments are in order:

1) The baseline case reported in Table 3 is really an average of the mixes 01–09 of Stephens et al. [1]. This is because the authors report little differences in the burn rates between mixes 01–09 when the AP is monomodal. To restate, changing the size of aluminum from 3 μm

Table 3 Table of mixes used in this study from [1][a]

	AP			Al		Binder
Mix	400	200	82.5	3	nm	
Baseline	——	67.50	——	20.00	——	12.50
	——	62.25	——	13.32	——	24.43
M10	——	53.84	13.46	20.00	——	12.70
	——	49.55	12.39	13.29	——	24.77
M11	——	40.38	26.92	20.00	——	12.70
	——	37.16	24.78	13.29	——	24.77
M12	——	26.92	40.38	20.00	——	12.70
	——	24.78	37.16	13.29	——	24.77
M13	53.84	——	13.46	20.00	——	12.70
	49.55	——	12.39	13.29	——	24.77
M15	67.30	——	——	20.00	——	12.70
	61.94	——	——	13.29	——	24.77
M17	——	53.84	13.46	17.00	3.00	12.70
	——	49.55	12.39	11.30	1.99	24.77

[a]The first row in the name of each mix corresponds to percentages by mass, and the second row gives the equivalent percentages by volume.

Table 4 Numerical representation of the propellant samples and packs

Mix	Edge, μm	Spheres	Grid, $N_x \times N_y \times N_z$
Baseline	1003	429	$81 \times 81 \times 52$
M15	1841	232	$121 \times 121 \times 52$
M12	715	902	$121 \times 121 \times 52$

to nano-size aluminum does not appear to alter the burn rate for monomodal 200-μm-diam AP; it does, however, change the strength of the propellant, certainly an important issue from a manufacturing point of view. Unfortunately, the authors kept the mass percent of aluminum fixed at 20%. It would have been extremely helpful had the authors done another study by changing the percentage of aluminum, thus providing data to investigate the effect of a change in aluminum content on the regression rate.

2) From burn-rate data regarding mixes M10, M11, and M12, we notice that decreasing the mass percentage of coarse AP (200 μm), and hence increasing the percentage of fine AP (82.5 μm), increases the burn rate at a fixed pressure.

3) We do not distinguish between fine (3 μm) and ultrafine (nanomicron) aluminum sizes. This means that we must exclude high pressures from our study, in which the actual size might play a role in the determination of burn rates.

Based on these considerations, we select the three morphologies indicated in Table 3 as baseline, M15, and M12 to conduct a comparison between the model and experiments. The edge of the cubic packs, the number of spheres, and the size of the computational grids are reported in Table 4. Note that the numbers in the last column of Table 4 refer to the gas-phase mesh only. The grids in the solid phase are chosen to be identical in size to those in the gas phase so that the number of total solution points doubles that based on reported dimensions.

B. Comparison of Experiments with Model Predictions

A comparison between experimental and computational burn rates is presented in Fig. 12. Computations are carried out for a set of pressures lower than in the experiments for three reasons:

1) The rationale is given in the third item of the previous list.

2) The chamber pressure of rocket motors for aerospace applications rarely exceeds 70 atm.

3) Numerical solution of the governing system of equations becomes considerably more stiff at high pressure, due to the reduction of the gas-phase length scale with an increase in burn rate. Both computations and experiments highlight that the burn rate versus pressure relation is a power law, and so computations for three pressures are considered sufficient to validate versus experiments.

The results of Fig. 12a show that the model predictions are in excellent agreement with measurements for the baseline case at all pressures. For the two other cases, the agreement is quantitatively poorer, with relative percentage error shown in Fig. 12d.

A comparison between the experimentally evaluated burning power law and the computationally evaluated analog is presented in Table 5. Qualitatively, the burning-characteristic trends displayed by the experiments are reproduced by the computations. M15 has a lower burn rate and a higher pressure exponent than the baseline case, whereas M12 has a higher burn rate than the baseline case. The model, therefore, correctly identifies the role of morphological scales on the burning characteristics of randomly packed propellant, but it tends to underestimate their importance on the regression rate-pressure correlation.

The propellant surface-temperature field and the radiation contribution to the energy equation, $-\nabla \cdot \boldsymbol{q}_r$, are shown for all three mixes in Table 4 and for the pressures of 22, 40, and 68 atm in Figs. 13 and 14. All of the plots refer to simulations for which at least one-half of the periodic pack's edge length (second column of Table 4) of propellant was burned, to clear out the initial inertial transient. The 3D surface snapshots show that the effect of the ambient pressure on the surface shape is consistent with that shown

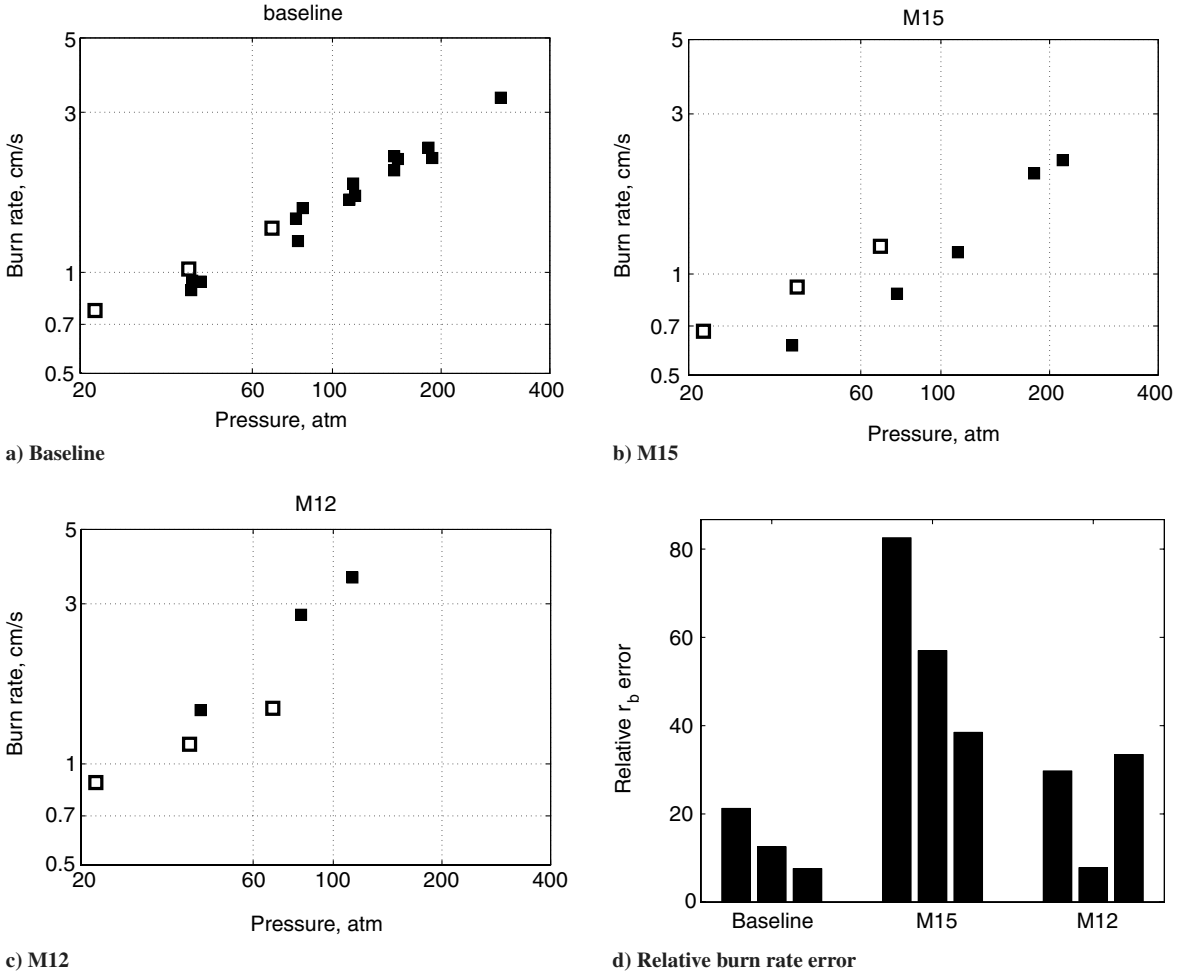

Fig. 12 Burn rate of randomly packed heterogeneous propellant: a–c) computations (open squares) compared with the experiments of Stephens et al. [1] (filled squares) and d) relative error between predictions and measurements (bars grouped under each pack denomination represent error evaluated at the three pressures of 22, 40, and 68 atm).

by the sandwich simulations (Fig. 10a), but the recession of the binder at high pressure in the 3D simulation is less accentuated than in the 2D simulations. This disparity is rooted in the multidimensional thermal distribution that supports heat conduction in 3D and in the fact that the thermal conductivity of the solid blends is markedly higher for the mixes of Table 3 than for those of Table 2 (used to determine the sandwich solid composition). Figure 13 shows that the difference in temperature between the binder and the AP increases with the pressure, a phenomenon linked to the different characteristic temperature of the pyrolysis laws associated with the two ingredients.

Figure 14 shows the radiative transport contribution to the local energy balance, $-\nabla \cdot \boldsymbol{q}_r$. In that figure, the field distribution is plotted on two planes, with coordinates equal to the maximum x and z values in the pack, together with the surface distribution. The conclusion is drawn that at low pressure, the radiative heat contribution is evenly distributed on the propellant surface. Such contribution is always positive at the surface and becomes negative over narrow pockets of high-temperature gas above the binder-surface regions. The distance of these pockets from the surface decreases with an increase in pressure. Correspondingly, the difference in radiative heat contribution between oxidizer and binder surfaces increases with the pressure.

Table 5 Empirical analysis of the burn rates[a]

Mix	Experiments A, cm/s	Experiments n	Computations A, cm/s	Computations n
Baseline	0.0994	0.60	0.16	0.5
M12	0.0231	1.08	0.22	0.46
M15	0.0353	0.76	0.13	0.52

[a]Here, $r_b = AP^n$, where A is in centimeters per second and pressure is in standard atmosphere (from Stephens et al. [1])

IX. Conclusions

The work we described in this paper centers around the derivation of a computational model for the deflagration of composite solid propellant with fine and ultrafine aluminum. The model is based on an Eulerian representation of the aluminum and aluminum-oxide concentration fields in the gas phase and a gray-medium approximation for the associated radiation field. The model is suitable for the analysis of heterogeneous multidimensional propellant deflagration.

The numerical experiments focused on the importance of aluminum burning and radiation on the deflagration process. An uncertainty parameter in the burning law of the aluminum particles [Eq. (60)] was introduced, due to the difficulty in extrapolating results for microscale particles to the nanoscale range. A parametric study was performed and the baseline case was identified by matching one-dimensional deflagration experiments. The calibrated model was extended to two-dimensional laminate propellant sandwiches with fine/ultrafine aluminum filled binder lamina. Steady-state computations showed that aluminum concentration has a marked impact on both surface shape and burn rate. The burn-rate augmentation of sandwich propellant is due to both the radiative heat feedback and the chemical energy release of the aluminum oxidation. The two phenomena manifest themselves with a significantly different distribution of heat feedback. The former leads to a large

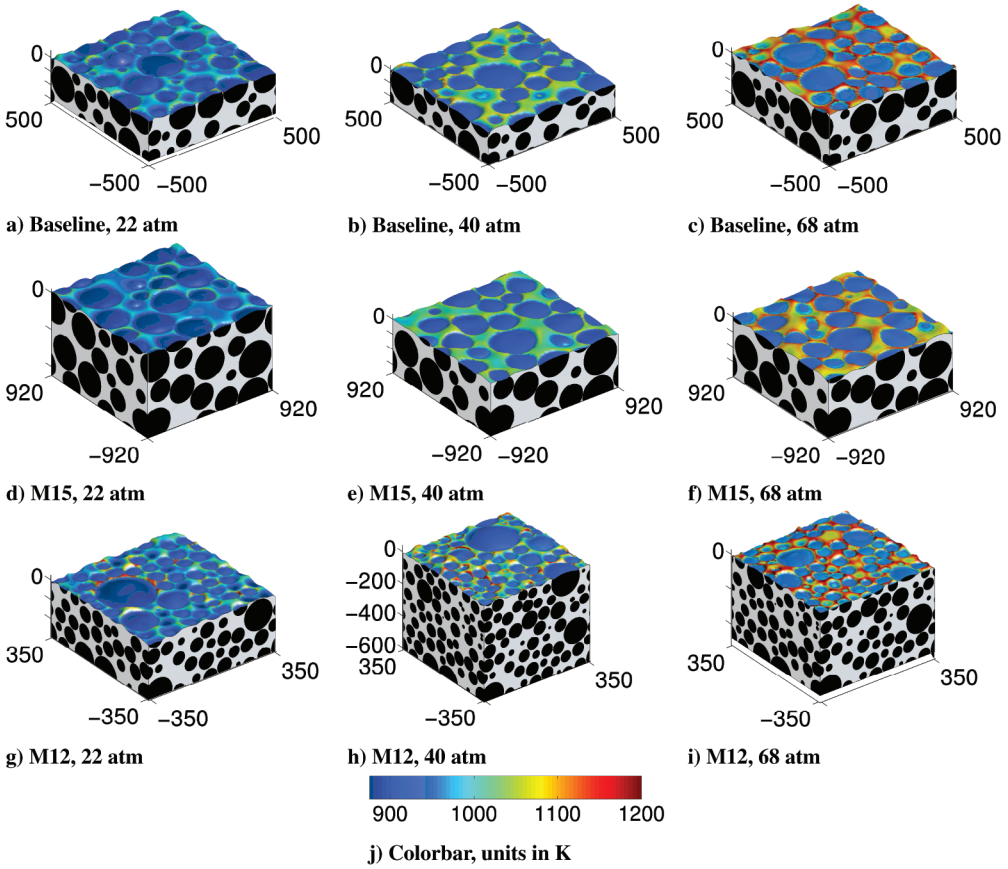

Fig. 13 Surface temperature of the randomly packed propellant mixes defined in Table 3; dimensions of the packs are in microns.

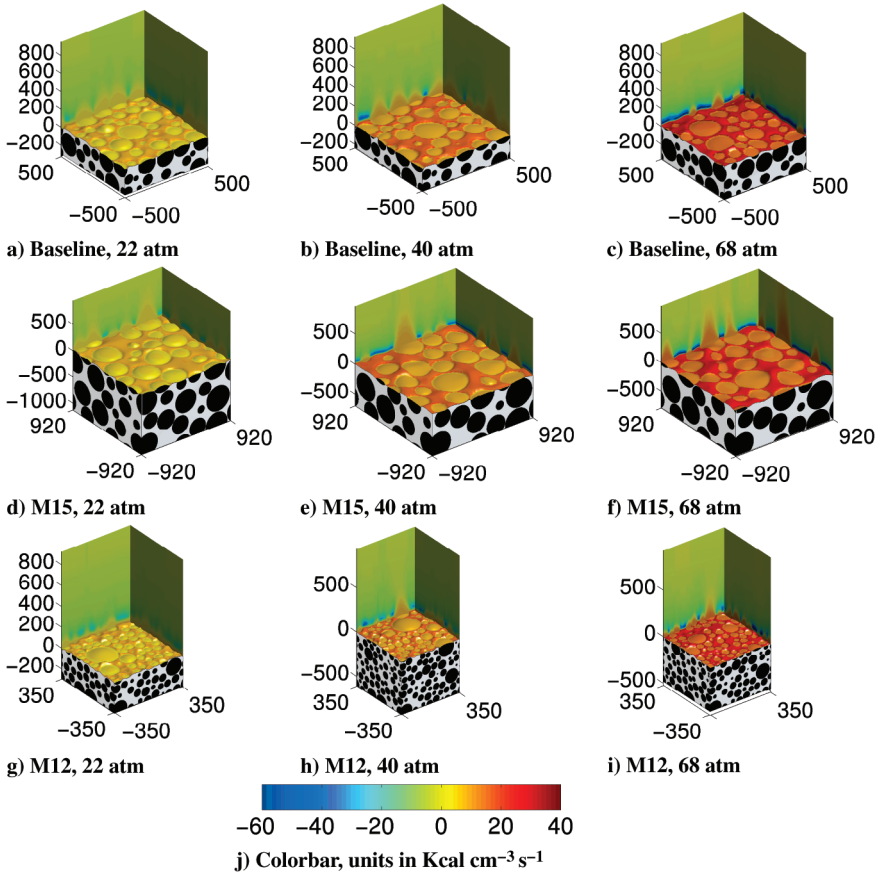

Fig. 14 Radiative contribution to the combustion filed supported by randomly packed propellant; the mixes are described in Table 3.

amount of heat feedback being conducted to the binder lamina, yielding a flat recessed binder. The latter yields a more uniform distribution, given the elliptic smoothness of the operator governing radiative transport. A pressure increase acts to reduce the effects of both radiation and aluminum oxidation on the thermal field, so that at large pressures ($P > 60$ atm), the combustion field is dominated by the oxidizer/fuel flame. Therefore, the binder recession diminishes with an increase in pressure, consistently with the reduced role of the diffusion flames.

The model was validated by comparing predictions of burn rate of randomly packed propellant with experiments. The model was shown to be very accurate for a monomodal pack with 200-μm AP particles, but it was significantly less accurate for a larger-particle case (400 μm) and for a bimodal distribution in which part of the 200-μm AP was substituted with a 82.5-μm distribution. Overall, the model identifies the qualitative trends linking burn rate to the morphology, but it underpredicts the magnitude of the morphology effect.

Future work will focus on the extension of the present model to include chemical mixture considerations into both the radiative property definitions and the aluminum oxidation, with the objective to improve the agreement of the comparison with experimental data. Future modeling efforts will also consider the addition of Lagrangian particles by a level set method to investigate the effect of microscale aluminum on the burning characteristics.

Acknowledgment

This research was supported by the U.S. Department of Energy through the University of California under subcontract number B523819.

References

[1] Stephens, M., Carro, R., Wolf, S., Sammet, T., Petersen, E., and Smit, C., "Performance of AP-Based Composite Propellant Containing Nanoscale Aluminum," 41st AIAA/ASME/SAE/ASEE Joint Propulsion Conference, AIAA Paper 2005-4470, 2005.

[2] Dokhan, A., Price, E. W., Seitzman, J. M., and Sigman, R. K., "The Ignition of Ultra-Fine Aluminum in Ammonium Perchlorate Solid Propellant Flames," 39th AIAA/ASME/SAE/ASEE Joint Propulsion Conference, AIAA Paper 2003-4810, 2003.

[3] Ishihara, A., Brewster, M. Q., Sheridan, T. A., and Krier, H., "The Influence of Radiative Heat Feedback on Burning Rates in Aluminized Propellants," *Combustion and Flame*, Vol. 84, No. 1, 1991, pp. 141–153. doi:10.1016/0010-2180(91)90043-B

[4] Brewster, M. Q., and Parry, D. L., "Radiative Heat Feedback in Aluminized Solid Propellant Combustion," *Journal of Thermophysics and Heat Transfer*, Vol. 2, No. 2, 1988, pp. 123–130.

[5] Jackson, T. L., Buckmaster, J., and Wang, X., "The Modeling of Propellants Containing Ultrafine Aluminum," *Journal of Propulsion and Power*, Vol. 23, No. 1, 2007, pp. 158–165. doi:10.2514/1.17493

[6] Modest, M. F., *Radiative Heat Transfer*, 2nd ed., Academic Press, New York, 2003.

[7] Massa, L., Jackson, T. L., and Buckmaster, J., "Optimization of Global Kinetics Parameters for Heterogeneous Propellant Combustion Using a Genetic Algorithm," *Combustion Theory and Modelling* (submitted for publication).

[8] Massa, L., Jackson, T. L., Buckmaster, J., and Campbell, M., "Three-Dimensional Heterogeneous Propellant Combustion," *Proceedings of the Combustion Institute*, Vol. 29, No. 2, 2002, pp. 2975–2983. doi:10.1016/S1540-7489(02)80363-7

[9] Jackson, T. L., and Buckmaster, J., "Heterogeneous Propellant Combustion," *AIAA Journal*, Vol. 40, No. 6, 2002, pp. 1122–1130.

[10] Wang, X., Jackson, T. L., Buckmaster, J., Massa, L., and Hossein, K., "Three-Dimensional Modeling of Aluminized Composite Solid Propellant Combustion," 42nd AIAA/ASME/SAE/ASEE Joint Propulsion Conference and Exhibit, AIAA Paper 2006-4927, 2006.

[11] Zhang, H., and Modest, M. F., "Evaluation of the Planck-Mean Absorption Coefficients from HITRAN and HITEMP Databases," *Journal of Quantitative Spectroscopy and Radiative Transfer*, Vol. 73, No. 6, 2002, pp. 649–653. doi:10.1016/S0022-4073(01)00178-9

[12] Najjar, F., Massa, L., Fiedler, R., Haselbacher, A., Wasistho, B., and Balachandar, S., "Effects of Aluminum Propellant Loading and Size Distribution in BATES Motors: A Multiphysics Computational Analysis," 41st AIAA/ASME/SAE/ASEE Joint Propulsion Conference, AIAA Paper 2005-3997, 2005.

[13] Mench, M. M., Kuo, K. K., Yeh, C. L., and Lu, Y. C., "Comparison of Thermal Behavior of Regular and UltraFine Aluminum Powders (ALEX) Made from Plasma Explosion Process," *Combustion Science and Technology*, Vol. 135, No. 1, 1998, pp. 269–292. doi:10.1080/00102209808924161

[14] Jones, D. E. G., Brousseau, P., Fouchard, R. C., Turcotte, A. M., and Kwok, Q. S. M., "Thermal Characterization of Passivated Nanometer Size Aluminum Powders," *Journal of Thermal Analysis and Calorimetry*, Vol. 61, No. 3, 2000, pp. 805–818. doi:10.1023/A:1010197115003

[15] Bazyn, T., Krier, H., and Glumac, N., "Shock Tube Measurements of Combustion of Nano-Aluminum," 44th AIAA Aerospace Sciences Meeting and Exhibit, AIAA Paper 2006-1157, 2006.

[16] Aita, K., Glumac, N., Vanka, S. P., and Krier, H., "Modeling the Combustion of Nano-Sized Aluminum Particles," 44th AIAA Aerospace Sciences Meeting and Exhibit, AIAA Paper 2006-1156, 2006.

[17] Widener, J. F., and Beckstead, M. W., "Aluminum Combustion Modeling is Solid Propellant Combustion Products," 34th AIAA/ASME/SAE/ASEE Joint Propulsion Conference, AIAA Paper 98-3824, 1998.

[18] Brandt, A., "Multi-Level Adaptive Solutions to Boundary-Value Problems," *Mathematics of Computation*, Vol. 31, No. 138, 1977, pp. 333–390.

[19] Saad, Y., and Schultz, M., "GMRES: A Generalized Minimal Residual Algorithm for Solving Nonsymmetric Linear Systems," *SIAM Journal on Scientific and Statistical Computing*, Vol. 7, No. 3, 1986, pp. 856–869. doi:10.1137/0907058

[20] Bazyn, T., Krier, H., and Glumac, N., "Oxidizer and Pressure Effects on the Combustion of 10-μm Aluminum Particles," *Journal of Propulsion and Power*, Vol. 21, No. 4, 2005, pp. 577–582.

[21] Mullen, J. C., and Brewster, M. Q., "Investigation of Aluminum Agglomeration in AP/HTPB Composite Propellants," 44th AIAA Aerospace Sciences Meeting and Exhibit, AIAA Paper 2006-280, 2006.

[22] Beckstead, M. W., Derr, R. L., and Price, C. F., "Model of Composite Solid-Propellant Combustion Based on Multiple Flames," *AIAA Journal*, Vol. 8, No. 12, 1970, pp. 2200–2207.

[23] Massa, L., Jackson, T. L., and Buckmaster, J., "New Kinetics for a Model of Heterogeneous Propellant Combustion," *Journal of Propulsion and Power*, Vol. 21, No. 5, 2005, pp. 914–924.

S. Son
Associate Editor